ETHzürich

Localization of Magnetic Field Disturbances using 3-Axis Magnetic Field Sensors

---

A Semester Thesis conducted at the Paul Scherrer Institute
by Iva Sanwald

supervised by
Jonas Manthey, Michael Marti, Mose Müller,
Dr. Cornelius Hempel and Prof. Jonathan Home

D-PHYS
ETH Zurich
Zurich, July 6, 2023

Abstract

In this thesis we present a three-dimensional magnetic field tracking system, motivated by the sensitivity of trapped ions to magnetic field disturbances. We start with the implementation of the data collection process for a set of three-axis magnetic field sensors, for two data transmission methods: via serial port, resulting in a low but constant sampling rate, and via WiFi with a high but inconsistent sampling rate up to $470\,\mathrm{Hz}$ for a single sensor. Next, we characterize two types of magnetic field sensor: the ICM-20948 from Invensense with a resolution of $\sim 600\,\mathrm{nT}$ and the MMC5983MA from MEMSIC with a resolution of $\sim 100\,\mathrm{nT}$. To measure changes in the magnetic field, we build a three-dimensional configuration of eight MMC sensors, the so-called 'Cube'. We test its performance and limitations using a rod magnet as controllable disturbance. In addition, we estimate the direction of the rod magnet position relative to the Cube by scaling the unit position vectors of the sensors with the measured magnitudes, respectively. The estimation method yields accurate results if the magnet is placed along one of the symmetry axes of the Cube. However, depending on the orientation and location of the magnet the estimated direction becomes less accurate. In the main text we will discuss further limitations of the setup and mention possible improvements.

1

Contents

1 Introduction

Historically, studies of magnetic phenomena date back to as early as 600 BC when the ancient Greeks discovered the attractive forces between lodestones and iron, and coined the word 'magnet'[1]. However, significant advancements in the theory of magnetism occurred much later after Oersted had discovered the connection between electric currents and magnetic forces in 1820 [2]. In comparison, the theory of electrostatics developed more rapidly, partly because electric fields arise from electric charges (monopoles), unlike magnetic fields which arise from tiny current loops (dipoles)[3].

Since the efforts of Oersted and his colleagues, magnets have become ever-present in our society. Sometimes plainly visible as kitchen magnets, children's toy or part of an industrial crane. But more often, as hidden element in appliances such as MRIs, credit cards, or computers. In the 20th and 21st centuries, researchers have consistently expanded our understanding of magnetism and developed methods to manipulate the magnetisation of nanoscale structures, including stable, single-atom magnets [4].

However, magnetic fields can also hinder new discoveries. In the pursuit of controlling ever smaller structures, we have entered a regime in which quantum effects play a crucial role. As a result, certain areas of research have become increasingly sensitive to minor disturbances in the surrounding magnetic field.

The measurement and localization of such small magnetic field disturbances is the focus of this project, motivated by their effect on the highly sensitive trapped ions at the Ion Trap Quantum Computing (ITQC) group at the PSI Quantum Hub. The ITQC group is part of a large number of research groups working towards the development of large scale quantum processors and the achievement of quantum advantage, when a quantum computer can solve a real-world problem faster than a classical computer. Even if these groups pursue the same goal, in many cases their implementation looks very different. The reason being the variety of possible two-state quantum systems that are suitable for the realisation of physical qubits[1]. For example, the vertical and horizontal polarization of a single photon, the two spin states of a spin-1/2 particle or two different energy levels in an atom [5].

The ITQC group utilizes two distinct energy levels of trapped Ca^+ ions as quantum states $|0\rangle$ and $|1\rangle$ in their physical realisation of qubits. As basic information unit of quantum computers qubits adhere to the laws of quantum mechanics and, once reliable enough, could provide computational advantage over classical computers for certain problems. However, their realisation presents numerous challenges. For example, changes in the surrounding magnetic field as low as $0.5\,\text{nT}$[2] can disturb their system and render labor-intensive calibrations useless. Hence, it is important to monitor the magnetic field as closely as possible and, in the event of a disturbance being registered, determine its direction to locate e.g. forgotten screwdrivers or identify opened drawers.

Considering these circumstances, we have developed a cubic configuration of magnetic

---

[1]Qubits are the basic information unit of quantum computers
[2]derived in section 2.1

field sensors, measuring the magnetic field at eight points in space and subsequently calculating the direction of a possible disturbance using a straightforward method we call 'scaling method'.

The rest of this thesis is structured as follows: First, we provide a more detailed explanation of how the experiments performed at the ITQC group are affected by external magnetic field disturbances, along with expressions for the magnetic dipole field and the field of a rod magnet. Next, we give an overview of the main hardware components and setup and explain how to read out data from multiple sensors and estimate the direction of a disturbance. We then test the resolution of two different 3-axis magnetic field sensors, referred to as 'ICM' and 'MMC', using a rod magnet with a known field as controllable disturbance. Finally, we analyse the performance of our three-dimensional sensor configuration and approximation method and provide ideas for applications and further improvements.

2   Theory

In this section, we first provide a brief explanation of the concept behind the trapped ions experiment of the ITQC group at PSI to highlight the importance of tracking magnetic field disturbances in their lab. At this point, we assume a basic knowledge of quantum mechanics, including a familiarity with the terms 'qubits' and 'superposition'. A great general introduction on quantum computing can be found in references [5] and [6]. In the second part, we introduce the magnetic dipole field and present an expression for the magnetic field of the rod magnet used in multiple experiments.

2.1   Trapped Ions at the ITQC Group

Simply put, the ITQC group uses two distinct energy levels of a ^{40}Ca$^+$ ion in a trapping potential[3] as computational basis states $|0\rangle$ and $|1\rangle$ of a qubit. They perform measurements and manipulations of the qubit state (general superposition of the basis states) with precisely calibrated laser beams, driving transitions between the states. For simplicity, we limit our discussion in this section to single trapped ions, but interested readers can find material on multiple ions in a single trap in references [6], [7], [8].

Now, let us take a closer look at the energy level structure of the Ca$^+$ ions to better understand how changes in the external magnetic field can disturb the carefully calibrated qubit. After a two-step ionization process[4], the ion inside the trap has a single remaining valence electron and an energy level structure similar to that of hydrogen [7]. The fine structure of the lowest three orbitals is illustrated in Figure 1, using the notation L_J where L denotes the total orbital angular momentum and J the total angular momentum. There

---

[3]linear Paul trap [7]

[4]In a first transition, a precisely calibrated laser ensures isotope selectivity. This is followed by the removal of the electron from the atom in the second step.[7]
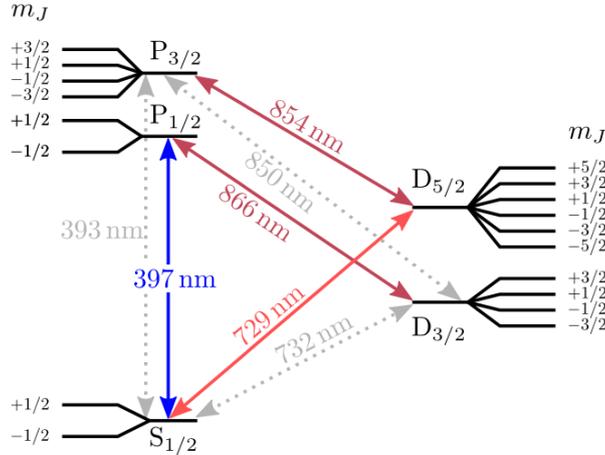
Figure 1: Energy level scheme of the Ca$^+$ ion. The 729 nm laser drives the transition between $|0\rangle$ (a Zeeman level of $D_{5/2}$) and $|1\rangle$ (a Zeeman level of $S_{1/2}$). Note, that not all combinations are possible. Due to the selection rules for electric quadrupole transitions we must satisfy: $\Delta m_j = 0, \pm 1, \pm 2$. More information on the other indicated transitions can be found in the source of this illustration: [8]

is an additional energy level degeneracy which is not lifted by the fine structure: the orientation of the total angular momentum, characterized by the quantum number m_j.

In an external magnetic field, this degeneracy is lifted via the so-called Zeeman effect. The Zeeman effect is based on the principle, that a magnetic moment $\vec{\mu}$ in an external magnetic field $\vec{B}$ has the additional magnetic potential energy $\Delta E = -\vec{\mu} \cdot \vec{B}$. In an atom, both the orbital motion and the intrinsic property 'spin' of electrons cause a magnetic moment, resulting in a total magnetic moment of the atom $\vec{\mu}$. Let us denote the direction of $\vec{B}$ as z-direction, $\vec{B} = B\hat{z}$. The z-component of the total magnetic moment can then be written as

$$\mu_z = -g_J \mu_B m_j, \tag{1}$$

with the Bohr magneton $\mu_B = e\hbar/2m_e$ and the geometric factor g_J, called Landé g-factor, which depends on the total angular momentum quantum number J. The projection of the total angular momentum onto the z-axis is characterized by the quantum number m_j, which can take values $m_j = -J, -J + 1, ..., J$. As a result, the energy of the interaction with an external magnetic field is

$$\Delta E = -\mu_z B = g_J \mu_B m_j B. \tag{2}$$

For every value of J there are $2J + 1$ possible values of m_j. Therefore, each fine structure level is split into $2J + 1$ so-called Zeeman levels, as illustrated in Figure 1.

If the external magnetic field at the trapped ion is disturbed, the splitting of the levels changes, shifting the frequency of the transition between two states. For example, the frequency shift $\Delta\nu$ of the transition $\left|S_{1/2}, m_j'\right\rangle \longrightarrow \left|D_{5/2}, m_j\right\rangle$, which corresponds to

$|1\rangle \longrightarrow |0\rangle$ for a possible combination of $m_j^{'}$ and m_j [5], is given by

$$\Delta \nu = \frac{\mu_B}{h} \left(g_{(D_{5/2})} m_j - g_{(S_{1/2})} m_j^{'} \right) \Delta B, \tag{3}$$

where ΔB is the change in magnitude of the magnetic field and $g_{(S_{1/2})} \approx 2$ and $g_{(D_{5/2})} \approx 1.2$ are the two Landé g-factors [7]. Such a shift in transition frequency causes an offset of the previously calibrated laser frequency. Depending on the line width of the natural transition and the laser, the performance of the setup is more or less sensitive to these offsets. For example, the $\left|S_{1/2}, 1/2\right\rangle \longrightarrow \left|D_{5/2}, 1/2\right\rangle$ transition has a natural line width of 0.15 Hz and the 729 nm laser driving this transition has a line width of approximately 1 Hz [8]. From Eq. 3, we get a shift of -5.6 Hz/nT in the transition frequency. Therefore, a disturbance of 0.5 nT at the trapped ion results in a laser frequency offset of 2.8 Hz. Depending on the type of experiment performed, this can be large enough to cause a significant drop in performance and possibly require a re-calibration of the laser.

2.2   Magnetostatic Fields

After highlighting the importance of measuring small magnetic field disturbances in the previous section, we are now providing a short derivation of the magnetic dipole field and the magnetic field of a rod magnet, which was used as a controlled disturbance in many experiments.

Magnetostatic fields $\vec{B}$ are described by Maxwell's equations

$$\vec{\nabla} \cdot \vec{B} = 0, \qquad\qquad \vec{\nabla} \times \vec{B} = \mu_0 \vec{J} \text{ (Ampere's Law)}, \tag{4}$$

where $\vec{J}(\vec{r})$ denotes the current distribution at position $\vec{r}$ and μ_0 is the vacuum magnetic permeability. The vanishing divergence of the magnetic field allows us to express $\vec{B}$ through a vector potential $\vec{A}$ as $\vec{B} = \vec{\nabla} \times \vec{A}$, but more importantly it implies the non-existence of magnetic monopoles. Contrary to the electric field with electric charges as elementary point sources, magnetic fields have no equivalent 'magnetic charge'. Instead, magnetic effects are attributed to currents, most elementary to infinitesimal current loops, i.e. tiny magnetic dipoles (Amperes Model)[9]. As we will see, this makes localizing magnetic field disturbances more complicated as they cannot be approximated as radial fields at large distances.

In the Coulomb gauge $\vec{\nabla} \cdot \vec{A} = 0$, Ampere's Law can be rewritten as $\vec{\nabla}^2 \vec{A} = -\mu_0 \vec{J}$, i.e. Poisson's equation with the general solution [9]:

$$\vec{A}(\vec{r}) = \frac{\mu_0}{4\pi} \int \frac{\vec{J}(\vec{r'})}{|\vec{r} - \vec{r'}|} \, d\vec{r'}. \tag{5}$$

We can simplify this expression in the case of a localized current distribution at large distances via the multipole expansion, based on the Taylor series of the term $1/|\vec{r} - \vec{r'}|$ for

---

[5]this is an electric quadrupole transition, i.e. selection rules allow transitions with $\Delta m_j = 0, \pm 1, \pm 2$ [7]

$r \gg r'$. We refrain from providing a detailed derivation of the expansion here, as it entails multiple steps and has been explained in great detail in numerous books (e.g. reference [9]). The relevant result, however, is that in first order, the vector potential is that of a magnetic dipole

$$\vec{A}_{dip}(\vec{r}) = \frac{\mu_0}{4\pi} \frac{\vec{m} \times \hat{r}}{r^2}, \tag{6}$$

where $\vec{m}$ is the magnetic dipole moment $\vec{m} = \frac{1}{2} \int (\vec{r} \times \vec{J}) \, d\vec{r}$ [9] and $\hat{r}$ is the unit vector in direction of $\vec{r}$. From this, we get an expression for a magnetic dipole field

$$\vec{B}_{dip}(\vec{r}) = \vec{\nabla} \times \vec{A}_{dip}(\vec{r}) = \frac{\mu_0}{4\pi} \frac{3\hat{r}(\vec{m} \cdot \hat{r}) - \vec{m}}{r^3}. \tag{7}$$

Important to note here is the dependency on the orientation of the magnetic moment relative to the position vector. If, for example, $\vec{m}$ points towards a magnetic field sensor, the registered magnitude is twice the magnitude we would have measured if the dipole was rotated by 90°.

Lastly, we derive an expression for the magnetic field of a rod magnet along its cylindrical axis, as such an object was used as controlled disturbance in our experiments. In magnetized material, the many atomic magnetic dipoles sum up to a total magnetic dipole moment per unit volume $\vec{M}$, known as magnetisation. The alignment of the internal dipoles can be effected by external magnetic fields. In some materials, so-called ferromagnets (e.g. iron), the dipoles remain aligned even after the magnetic field is removed, resulting in a remaining magnetic field or remanence B_r [9]. From this, the field along the cylindrical axis of a rod magnet can be calculated as

$$B = \frac{B_r}{2} \left(\frac{h + z}{\sqrt{R^2 + (h + z)^2}} - \frac{z}{\sqrt{R^2 + z^2}} \right), \tag{8}$$

where z denotes the distance from the north pole of the magnet along the cylindrical axis, h its height and R its radius [10].

3 Setup

This section gives an overview of the main hardware components and presents the three-dimensional sensor configuration ('the Cube') built to track changes in the magnetic field.

3.1 Hardware

In all experiments the setup consists of multiple 3-axis magnetic field sensors connected to a microcontroller via the serial communication protocol I^2C. This protocol enables the communication of the controller device (the microcontroller) with multiple peripheral devices (the sensors). I^2C uses two lines, the serial data (SDA) to send and receive data and the serial clock line (SCL) carrying the clock signal. To ensure that data is exchanged between
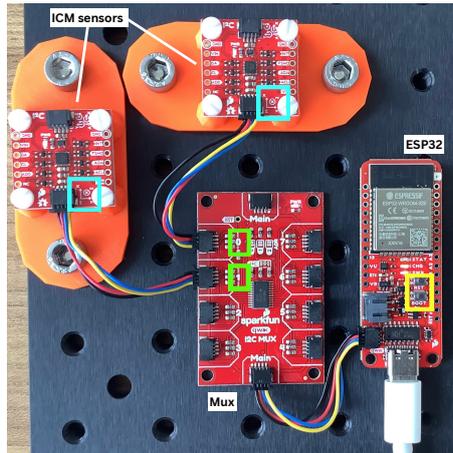
Figure 2: Setup example with Mux, ESP32 and ICM sensors. Green: port numbers, Blue: sensor coordinate system, Yellow: Reset/Boot buttons.

the correct two devices, each peripheral on the bus has a 7-bit address which is transmitted at the beginning of every message. As all of our magnetic field sensors share the same address [6], a multiplexer (Mux) with 8 ports was added in between the microcontroller and the sensors to manage the communication between the devices (Figure 2). We ordered all our components from SparkFun, such that the sensors and the microprocessor are on Spark-Fun breakout boards and part of their Qwiic Connect System. This system enables the connection of I²C devices without soldering using polarized Qwiic cables and connectors. It includes a wide variety of development boards, sensors, accessory boards and shields [11].

Microcontroller: We used the ESP32 WROOM Thing Plus microcontroller from SparkFun ('ESP32'). The ESP32 board houses an Xtensa single-core 32-bit LX6 microprocessor, with 448KB of ROM and 520KB SRAM. Its features include:

- 21 multifunctional GPIOs;

- integrated WiFi 2.4GHz transceiver

- USB-C connector (used for establishing serial connection and power)

- Qwiic connector (used to connect to the sensors/Mux)

- 4 LEDs

- 2 buttons: Reset (RST) and Boot (BOOT)

More specifications can be found in the data sheet [12].

---

[6]All sensors of type ICM can be assigned one of two addresses 1101000 or 1101001 [13], while all sensors of type MMC have the same 7-bit address 0110000 [14].

Table 1: Sensor Specifics. Direct comparison of the ICM and the MMC sensor, based on the two data sheets provided by SparkFun.

	ICM [13]	MMC [14]
Field Range (each axis)	$\pm4900\,\mu T$	$\pm800\,\mu T$
Output Resolution	16-bit	18-bit
Sensitivity Scale Factor	$0.15\,\mu T/LSB$	$6.25\,nT/LSB$
RMS Noise	-	$0.04\,\mu T$
Max. Output Data Rate	$100\,Hz$	$1\,kHz$
Null Field Output	$\pm300\,\mu T$	$\pm50\,\mu T$
Magnetic Sensor Type	Hall-effect	AMR

Magnetic Field Sensors: Over the course of this project, we tested two different 3-axis magnetic field sensor breakout boards from SparkFun: the 9DoF IMU Breakout Board with Invensense's ICM-20948 Sensor (referred to as 'ICM') and the MMC5983MA sensor (referred to as 'MMC') from MEMSIC. Table 1 presents a direct comparison of the two sensor specifications. Despite their large initial calibration uncertainty, we did not calibrate the sensors as we are interested in the change of the magnetic field between measurements, rather than its value at a specific time.

We started with the ICM breakout board, a 9-axis motion tracking device including a 3-axis silicon monolithic Hall-effect magnetic sensor, a 3-axis gyroscope and a 3-axis accelerometer. The device can be assigned one of the two I^{2}C addresses 1101000 and 1101001. Its magnetometer has a measurement range of $\pm4900\,\mu T$ and an output data resolution of 16-bit. [13]

After testing the performance of the ICM device, we switched to the MMC sensor. It is an Anisotropic Magneto-Resistive (AMR) sensor made from a thin permalloy film deposited on a silicon wafer. The film exhibits a magnetisation-dependant characteristic resistance. Using the measured changes in resistance, the strength of the external magnetic field can be inferred. However, the film's characteristics can change in magnetic fields above $1\,mT$. To clear the film of any residual magnetic polarisation the MMC has a built in set/reset operation, which utilizes a strong current to reset the film's characteristic. Apart from using a different measuring technique, the MMC sensor also performs differently. While its measurement range is limited to $\pm800\,\mu T$ and it can only be assigned the I^{2}C address 0110000, it has a higher resolution of 18-bit and a ten times higher data output rate of $1\,kHz$.[14]

Multiplexer: The SparkFun Qwiic Mux Breakout ('Mux') enables the communication between the controller device and up to eight peripherals with the same I^{2}C address. In the case of the ICM sensors, we can daisy chain two sensors to each port of a Mux, as they are assigned one of two addresses. The Mux itself has eight configurable addresses, such that a total of 128 ICM sensors or 64 MMC sensors can be connected to the microcontroller. However, the greater the number of sensors, the lower the measurement frequency for each
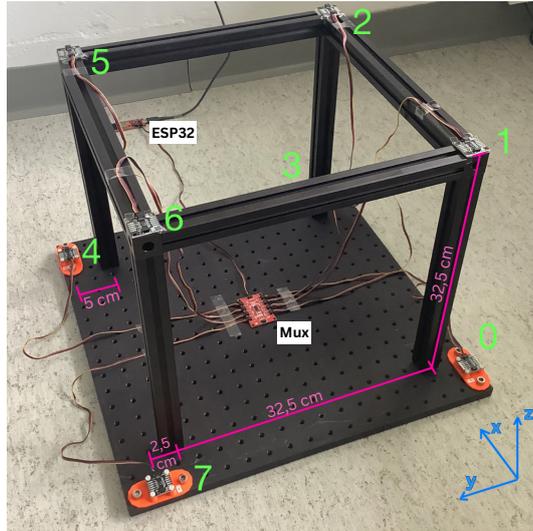
Figure 3: 3D setup of 8 MMC sensors ('Cube'). The green numbers indicate which Mux port the respective sensor is connected to. Sensors 1, 2, 5 and 6 are fixed at the corners of the aluminium structure. The lower sensors 0, 3, 4 and 7 cannot be positioned exactly at the corners and therefore have been placed with an offset in x and y direction such that the positioning of the sensors is symmetric under 90° rotations around the z-axis.

sensor. For a large number of sensors, it is therefore advisable to change from a ESP32 to a device with more RAM, e.g. a Raspberry Pi, or use multiple devices.

3.2 3D Sensor Configuration - 'The Cube'

Aside from multiple smaller setups, which are introduced in later sections, we used one main three-dimensional configuration of magnetic field sensors. The configuration illustrated in Figure 3 ('the Cube') features eight MMC sensors affixed to an aluminium rod-constructed cube, positioned above an optical breakout board. The upper four sensors are mounted to the corners of the cube, whereas the sensors on the lower level are placed with a slight offset as indicated in the picture.

4 Methods

In this chapter, we will give an overview of our data collection process [7] and briefly explain the calculation of the change in the magnetic field from our measurements. In addition, we will demonstrate a straightforward technique for estimating the direction of a magnetic dipole relative to the Cube and simulate its performance for a two-dimensional sensor configuration.

---

[7]We limit our explanation to the code for the MMC sensors as they turned out to be more suitable for this project. Data acquisition with the ICM sensors works similarly but with different sensor libraries.

4.1 Data Collection Process

The data acquisition relies on the interplay between a Python script, running on an external computer, and a C++ sketch deployed on the ESP32. The role of the ESP32 involves collecting magnetic field measurements from the sensors connected to the Mux and transmitting them to the computer. The Python script functions to accept data from the ESP32 and save it as CSV file. Over the course of this project, we switch between two different interaction modes: serial communication and WiFi. This allows us to choose whether to prioritize a continuous data flow or a high sampling rate. The subsequent sections provide a detailed description of the scripts for both methods on the basis of the flowcharts in Figure 4 and highlight limitations and differences.

4.1.1 Serial Communication

In the serial communication mode, the microcontroller continuously iterates through all the sensors connected to the Mux and sends the magnetic field data for all three axes to the receiving computer using the serial connection. By opening and closing the serial port via a Python script, one can control when data is received and subsequently stored as a CSV file.

Code on Microcontroller: Every sketch on the ESP32 (see Figure 4) mainly consists of two functions, one of which performs the setup step, and the other one being the main loop. The setup is triggered either through manually pressing the RST button on the board or setting the DTR ('Data Terminal Ready') state when opening the serial port in Python. The function starts with a number of initialisations, including the serial port, the sensors and the Mux. Next, it initialises the communication with the sensors and the Mux by assigning each sensor object to a port on the Mux and performing the built-in reset operation on all sensors to get rid of any residual magnetisation. Due to the strong current applied during this operation, a delay time of half a second is necessary to ensure that the subsequent measurements are not affected by magnetic induction.

Following the execution of the setup function, the loop function continues to be executed (repetitively) until either the board is reset or the power supply is disconnected. In each run, the time is taken in milliseconds relative to the last reset and send to the computer via serial port. Then, the function loops over all the sensors by selecting the correct port number of the Mux and measures the magnetic field along three axes. The initial data values are unsigned integers (referred to as 'counts') and need to be converted to values of the magnetic field in μT. As the MMC sensors have a range of ±800 μT and a 18-bit output resolution this is achieved with

$$B_i = \frac{(Z_i - 2^{17}) \cdot 800 \, \mu\text{T}}{2^{17}}, \tag{9}$$

where B_i denotes the magnetic field along one axis, Z_i the counts returned by the sensor, and 2^{17} corresponds to the mid point of the 18-bit integers. For a range of ±800 μT the mid point corresponds to the value 0 μT. The converted values are then transmitted
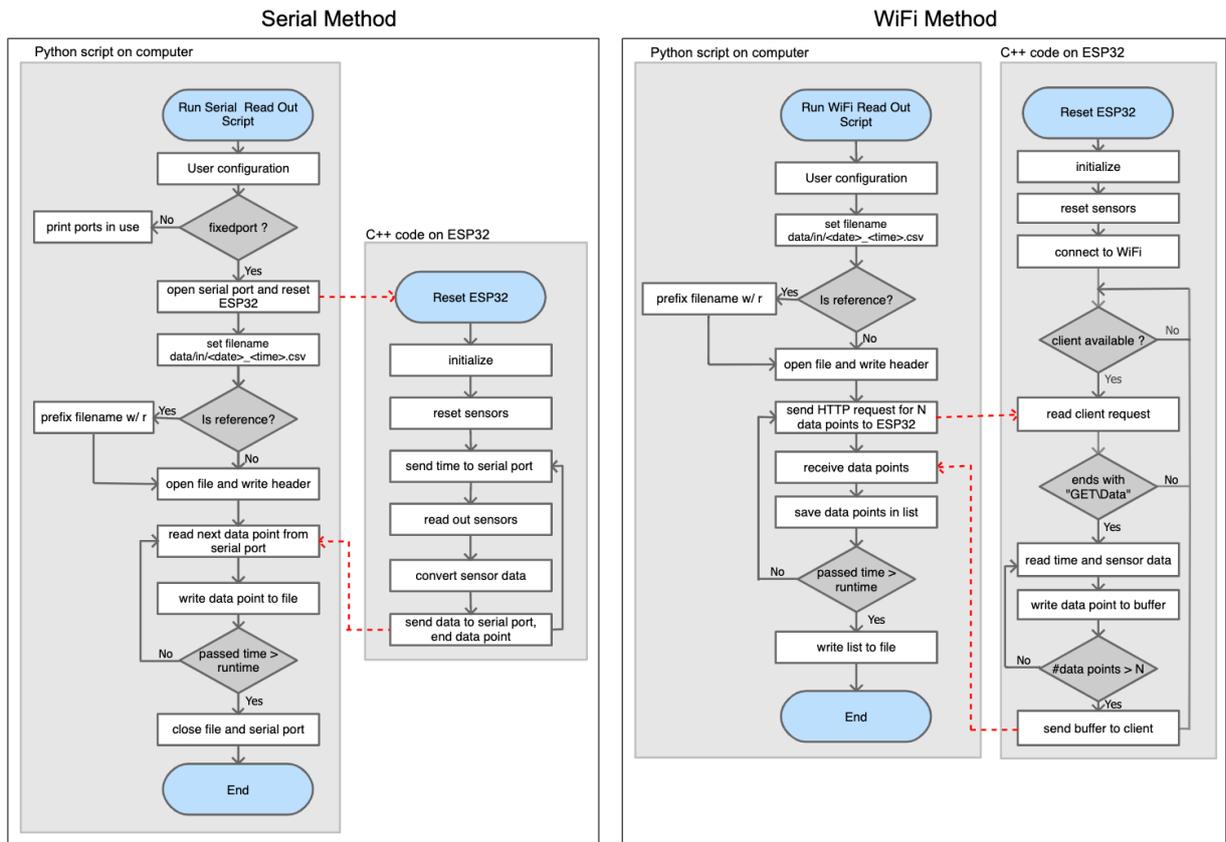
Figure 4: Flowcharts of the C++ code (ESP32) and the Python script (external computer) for both communication methods. When running an experiment one can choose between either method but first one has to upload the corresponding code onto the microcontroller, as the ESP32 can only save one program at a time. The red lines indicate communication between the two devices.

through the serial port to the connected computer, with a new line character following each transmission. Hereafter, we will define a set of one timestamp followed by one measurement per axis and sensor as 'one data point'.

Python Script: The Python script first performs some configuration settings, including the number of sensors, the duration for which the script will run, the data type[8] (either reference data or raw data) and the serial port address on the computer. If the port is not known, one can print out the ports in use by setting `fixedport = False`. Next, the ESP32 is reset and the serial port is opened starting the communication with the ESP32. The Python script reads the data coming from the ESP32 through the serial port and writes it into a CSV file for the specified time interval.

4.1.2 WiFi

In this section, we will present an alternative way of transferring data from the ESP32 to the computer using WiFi. The main idea is that the microcontroller acts as a server, waiting for new data requests, while the sensors are continuously measuring at a rate of 1kSpS (kilo Sample per Second). If connected to the same network as the ESP32, data can be requested via a HTTP request, i.e. hypertext transfer protocol message, starting with 'http:'. 'Measuring the magnetic field' then comes down to running a Python script which repeatedly sends data requests to the ESP32 and writes the returning data into a CSV file.

Code on Microcontroller: The basic structure of the code is the same as for serial communication, so we will only highlight the differences. After the initialisation and sensor resets, the ESP32 is connected to a WiFi network. In the loop function, the server object listens for incoming connections. Upon receiving a `GET` request at the '`\Data`' endpoint, the code triggers the execution of the transmission process. Going through the ports on the Mux, the unconverted data of each sensor is read and saved in a buffer on the ESP32. Conversion of the values to μT is performed later during the data analysis on the computer to make the code on the ESP32 faster, allowing higher sampling rates. When the buffer is filled with a certain number of data points, the data is send to the client. The number of data points taken per client request can be adjusted but is limited by the 520KB SRAM of the ESP32. For example, the limit with 8 sensors connected to the Mux is 33 data points per request, see Table 2.

Python Script: The Python script for the read out via WiFi is very similar to the one for serial communication. The main difference is, that data is received via HTTP requests `http://X.X.X.X/Data`, with `X.X.X.X` being the IP address of the ESP32.

---

[8]This is important, as reference files are prefixed with an 'r' so they can be distinguished from raw data files later. More about reference data vs. raw data can be found in section 4.2

Table 2: WiFi method limitations. Experimentally determined limitations of the WiFi communication method. *sensors:* Number of sensors connected to the Mux. *data points/request:* Maximum number of data points per request, limited by ESP32 RAM. *frequency:* Number of data points per second. *data time frame:* Time frame per request with data points. *dead time:* Time without data points during transmission. Errors: Standard deviation of data sets with approx. 100 entries each.

sensors	data points/request	frequency [Hz]	data time frame [ms]	dead time [ms]
1	212	469.4 ± 0.5	451.6 ± 0.5	548.3 ± 92.2
2	120	235.7 ± 0.2	509.1 ± 0.3	427.0 ± 106.6
4	64	118.73 ± 0.04	539.0 ± 0.2	325.7 ± 96.7
8	33	60.27 ± 0.05	547.6 ± 0.5	341.1 ± 159.0

4.1.3 Comparison

The WiFi method is much faster than the serial port transmission, with an average data point frequency of approximately 470 Hz, compared to 100 Hz for a single MMC sensor. In addition, this method does not rely on a cable for data transmission to an external device, making the placement of the setup more flexible and removing the cable as possible source of error. However, the limited memory of the ESP32 leads to varying time intervals between data points. For example, 8 sensors connected to the Mux have a limit of 33 data points per request before the buffer on the ESP32 is full and the data has to be send to the client. Hence, we have a time frame of $\sim 0.55\,$s with data points at a high, constant frequency followed by a window of $\sim 0.35\,$s without data during the transmission process, referred to as 'dead time'. The maximum number of data points per request, the frequency and the dead time for different numbers of MMC sensors connected to the ESP32 can be found in Table 2. This problem does not occur with the serial communication method, where data is sent at a lower, but constant frequency.

Considering that trapped ion experiments at the ITQC group are performed at a time scale of a few milliseconds, neither the serial communication method nor the WiFi method are fast enough for tracking changes over the course of a single experiment. However, there is potential to increase the data point frequency of the WiFi method as the sampling rate of a single MMC sensor is 1 kHz according to the data sheet [14].

4.2 Calculating Magnetic Field Changes

After focusing on the data acquisition in the previous sections, we now explain how we track changes in the magnetic field.

Simply put, tracking changes requires two sets of data taken at different points in time, referred to as reference data and raw data. When testing the performance of our sensor setup, we require the disturbance of the magnetic field between reference and raw measurements to be limited to the effects of a test magnet as much as possible. However,

the uncontrollable environment [9] reduced the reliability of such a reference measurement with time, such that a new reference measurement has to be taken for every set of raw data.

One reference measurement consists of a few hundred data points taken over a short period of time while keeping the field as stable as possible. By subtracting the temporal average of these data points from the array of raw values, we are left with the change in the magnetic field vector over time at each sensor position. In most experiments, we make the assumption of a static disturbance and average the change in the magnetic field vector over the duration of the raw measurement.

4.3   Approximation of Disturbance Direction - Scaling Method

As mentioned before, our goal is not only to measure disturbances in the magnetic field but also to derive the direction of its source from the measurements of the eight sensors on the Cube.

In a first approximation, we are treating any disturbance as magnetic dipole field, motivated by the multipole expansion in section 2.2. Even after making this approximation, the problem remains defined by a set of eight non-linear equations (magnetic dipole field Eq. 7), which we will not attempt to solve numerically. Instead, we opt for a straightforward localization method based on the following approximation. We consider only the magnitude of the magnetic field and assume that sensors closer to the disturbance detect a larger change in magnitude. Herein lies a significant simplification, as we disregard the orientation of the magnetic dipole relative to the sensor.

Based on these approximations, we estimate the direction of the source by scaling the unit vectors pointing from the center of the configuration towards the sensors with the measured magnitudes, respectively, and then normalizing the sum of the re-scaled vectors. Hereafter, this approximation method will be referred to as 'scaling method'. To characterize the performance of this method, we simulated a magnetic dipole being placed at different locations close to a two dimensional setup of four ideal[10] sensors placed at the corners of a 30 cm x 30 cm square. Note that, in this simulation, the magnetic dipole always points towards the origin, i.e center of the square. Figure 5 visualizes the deviation of the direction according to the scaling method from the actual position of the magnetic dipole in degrees up to a distance of 50 cm from the center.

Considering the approximations we made, the scaling method yields surprisingly accurate results for this configuration, with a maximal deviation of ± 16 degree close to the setup. In addition, the simulation suggests very accurate results along the symmetry axes of the setup, showing 0 degree deviation. It is worth mentioning that the results in Figure 5 are valid for all magnetic dipoles. This is because the scaling method scales vectors linearly with the magnitude of the magnetic field, which, in turn, is proportional to the magnetic dipole moment according to Eq. 7.

---

[9]We found that, for example, the position of chairs in the room, some shoes, and cables influenced the
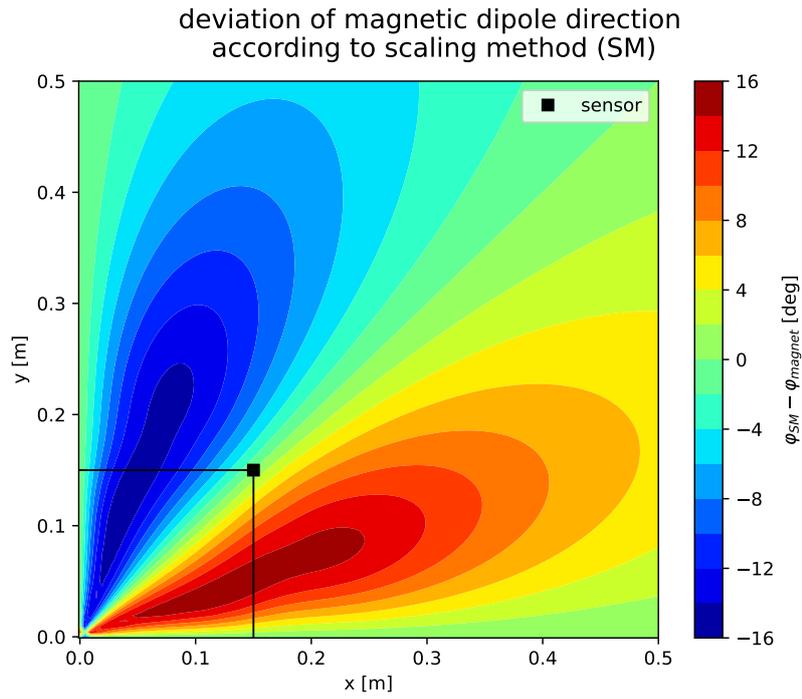
Figure 5: Simulation of the scaling method for four sensors placed at the corners of a 30 cm x 30 cm square. We assume that the sensors measure the magnetic field with perfect accuracy. The origin of the coordinate system is placed at the center of the square and due to symmetry, only the first quadrant is simulated. For each point on a 200 x 200 grid we calculate the direction according to the scaling method for a magnetic dipole placed at this position pointing towards the origin. The colors indicate the deviation between the polar angle of the scaling method vector and the actual position vector of the dipole.
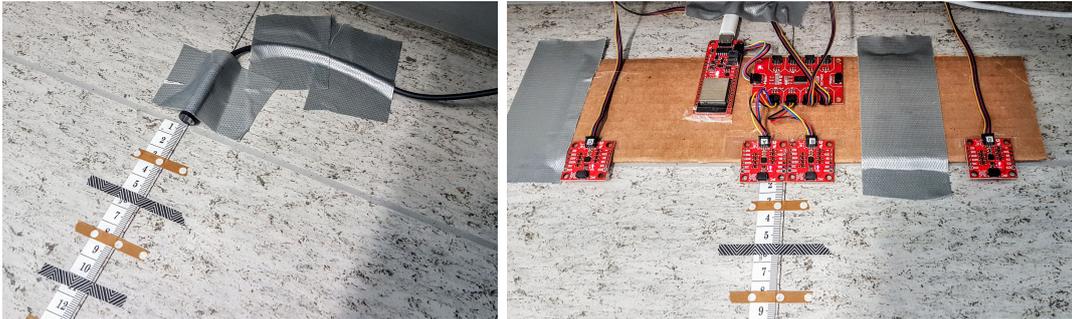
Figure 6: *Left:* Setup of the fluxmaster to measure the magnetic field of the test magnet along the black string at various distances. *Right:* Setup of four ICM sensors, the microcontroller and the Mux to test the sensor performance by placing the test magnet on the black string at various distances. The experiment was repeated with the MMC sensors.

5   Sensor Characterization

The purpose of this section is to evaluate the performance of the ICM and MMC sensors by utilizing a rod magnet as a controllable disturbance. To achieve this, we conducted measurements of the magnetic field along its cylindrical axis at different distances and compared the results with the theoretical field calculated based on the fabrication details of the magnet. For all our experiments, we used the S-06-13-N magnet (also referred to as 'test magnet' or 'rod magnet') ordered from supermagnete.ch.

5.1   Checking Magnet Fabrication Specifications

First, we verified the provided magnet specifications by measuring the magnetic field along the cylindrical axis of the magnet at various distances using the fluxmaster magnetometer from Stefan Mayer Instruments ('fluxmaster')(see Figure 6). We then compared the measured values to the theoretical field calculated using Eq. 8 with radius $r = 3\,\mathrm{mm}$, height $h = 13\,\mathrm{mm}$, and magnetisation N48 [16], i.e. residual magnetisation $B_r = 1.37 - 1.42\,\mathrm{T}$ [17]. Looking at the results in Figure 7, there seems to be a systematic error, as all data points lie below the theoretical curve. This offset may be attributed to a lower residual magnetisation B_r than what is indicated in the data sheet. However, when fitting the data using Eq. 8 with B_r as a parameter, we observe a deviation of over 30% from the theoretical value. A more likely cause is a systematic error due to our experimental setup or measuring method. It may be that the one side of the measuring tape used to align the fluxmaster with the magnet axis did not start at the center of the fluxmaster, resulting in a constant shift of the fluxmaster axis perpendicular to the axis of the magnet. Then, at large distances the axes would still be aligned while at short distances the shift causes a larger misalignment, explaining why the offset is more pronounced at shorter distances.

---

magnetic field enough to effect the calculation of the field disturbance

[10]measure the magnetic field with perfect accuracy
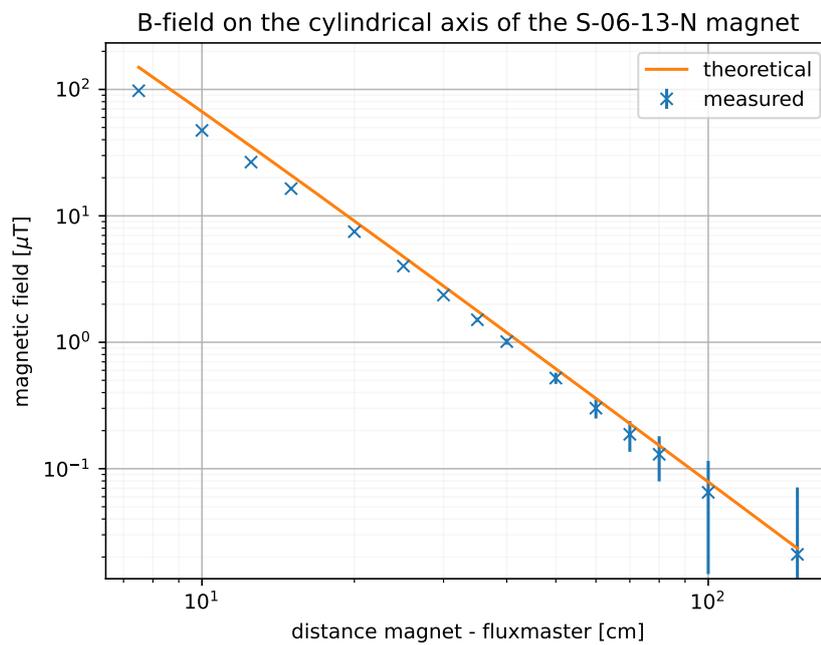
Figure 7: Comparison of the theoretical magnetic field along the cylindrical axis of the test magnet and the change in the magnetic field measured with the fluxmaster at various distances from the magnet. The errors are the result of the 0.5 % accuracy and $< 5\,\mathrm{nT}$ offset stated in the data sheet of the fluxmaster [15] and an uncertainty of $50\,\mathrm{nT}$ due to fluctuations in the readings during the experiment.

5.2 Testing Sensor Sensitivity

To test the performance of the two different types of magnetic field sensors, we repeated the following experiment with both sensor sets (see Figure 6 on the right).

We positioned four sensors perpendicular to a measuring tape on the floor and connected them to the Mux and microcontroller. In this experiment, we used the serial communication method to prioritize a continuous flow of data, rather than a high sampling rate. Initially, we conducted a reference measurement lasting for 7 s, with the magnet placed at a distance of more than 3 m away. Subsequently, we positioned the rod magnet parallel to the measuring tape, at a distance of 2.5 cm from the sensor line on the black string, and performed another measurement for 7 s. We repeated this process for multiple distances up to 150 cm and calculated the changes in the magnetic field each time as outlined in section 4.2.

The results for the inner sensors 0 and 1 are presented in Figure 8. They demonstrate that the MMC sensors are capable of detecting changes in the magnetic field as low as approximately 100 nT, while the ICM sensors reach their limit at around 600 nT. This difference in resolution is essential when trying to measure small magnetic field disturbances in a lab: we measured a magnetic field disturbance of (408 ± 14)nT[11] when pointing a screwdriver at the MMC sensor setup 50 cm away, which is outside the resolution range of the ICM sensors. Note, that the experiments at the ITQC group can already be disturbed by changes of 0.5 nT at the ions. However, they will install a magnetic shield around their setup reducing the effect of external magnetic fields.

Moreover, the results obtained at medium distances are in good agreement with the theoretically calculated field (Eq. 8), confirming that the magnet specifications agree with the indicated fabrication specifics. We attribute the deviation from the theoretical values observed at small distances to the sensors being positioned 1.25 cm away from the cylindrical axis due to limitations in the setup (see Figure 6). Furthermore, at a distance of 2.5 cm, the magnetic field along the cylindrical axis exceeds the range of the MMC sensors, leading to an underestimation of the magnitude of the magnetic field at that distance.

5.3 Measurement Distribution

To verify our assumption of normally distributed measurement noise in our data, we analysed the data obtained from the ICM and MMC sensors during a 30 s measurement in a stable external magnetic field[12]. The results, illustrated in Figure 9, display a normal distribution for two randomly chosen sensors, one ICM and one MMC. It is important to note that the sensors have not been calibrated, meaning that the values in the plots do not accurately represent the actual magnetic field values. They include an unknown offset for each axis and sensor.

---

[11]averaged result of the two inner sensors 0 and 1.

[12]The magnetic field was not perfectly stable, but we can rule out any large drifts, as we monitored the field along the x-axis during the measurement with the fluxmaster.
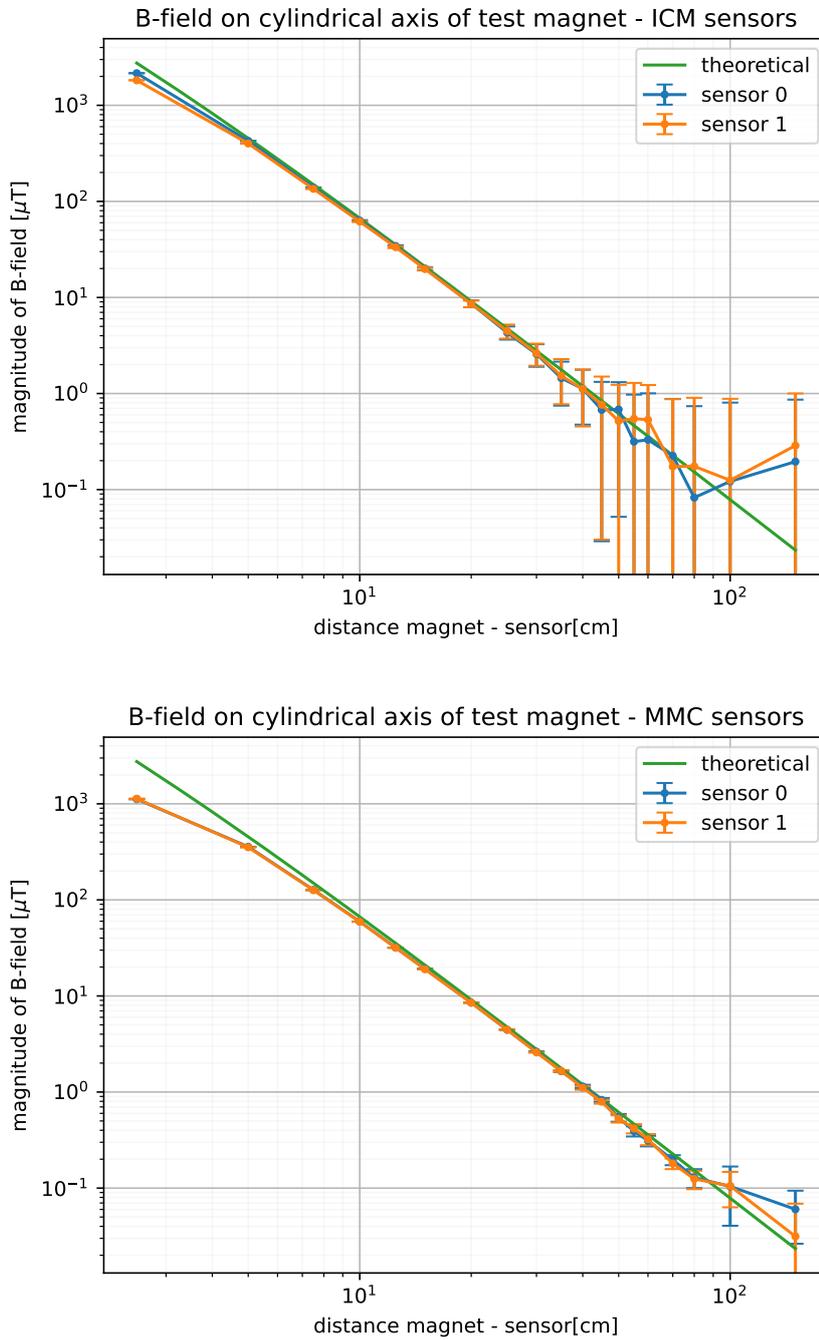
Figure 8: These plots show the magnetic field magnitude of the test magnet measured at various distances with the setup depicted in Figure 6 on the right. The errors on the magnitude are calculated from the standard deviation of the 7 s reference and raw measurements along each axis using Gaussian error propagation. *Top:* Results for the ICM sensors. *Bottom:* Results for the MMC sensors
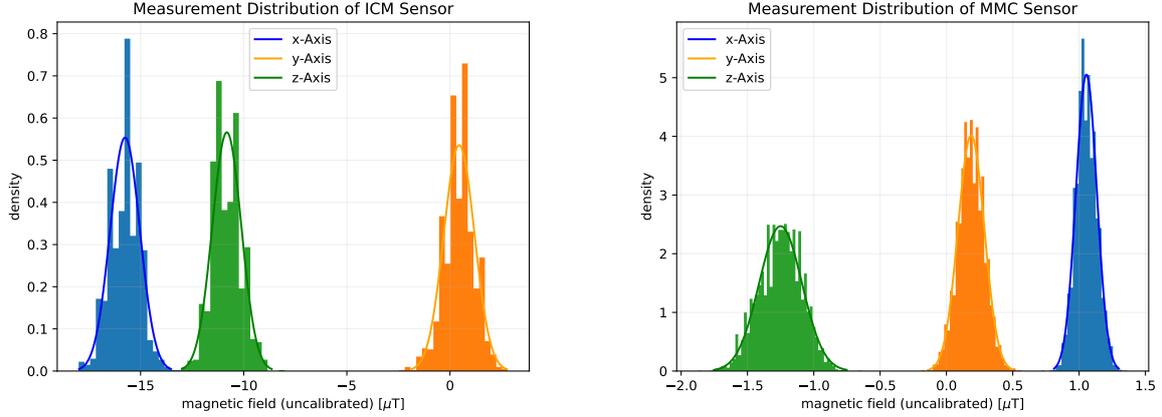
Figure 9: Distribution of data during a 30 s measurement in a stable external magnetic field for two randomly chosen sensors together with a Gaussian fit. All six histograms are individually normalized such that the area under the histogram yields 1. The sensors have not been calibrated. *Left:* ICM sensor, 1473 data points, *Right:* MMC sensor, 6572 data points.

5.4 Detecting Disturbances at 50 Hz

The objective of this experiment is to detect periodic changes in the magnetic field at 50 Hz using a single MMC sensor. This frequency is especially interesting, as many AC sources/devices, such as power sockets or voltage transformers operate at 50 Hz. We conducted magnetic field measurements for three different setups: background measurement, voltage transformer in standby next to the sensor, and voltage transformer with a running heating plate next to the sensor. In each setup, we performed 20 measurements lasting for 2 seconds using the WiFi transmission code, with 200 data points per request, allowing us to achieve a sampling frequency of approximately 500 Hz and capture frequencies up to 250 Hz in the signal. Then, we applied a discrete Fourier transform using `scipy.fft.rfft` and analysed the spectrum averaged across all 20 measurements.

The results displayed in Figure 10 clearly indicate the presence of signals at 50 Hz and 160 Hz. Interestingly, the amplitude of the signal at 160 Hz remained consistent across different setups and was also observed in other experiments conducted at various locations. This observation suggests that the microcontroller, the Mux, and the sensors themselves are the probable sources of this signal. In addition, the 160 Hz signal is most prominent along the z-axis. This could be the reason, why the z-axis variance of the MMC sensor in Figure 9 is larger than the x-axis and y-axis variance.

The presence of the 50 Hz signal during the background measurement is most likely the result of the aforementioned alternating current in power sockets. Additionally, if we examine the amplitude difference between the spectrum of the background measurement and the voltage transformer in standby, we can identify a significant peak at 50 Hz for axis x and z. Therefore, the sampling rate of a single MMC sensor using the WiFi method is

21

Figure 10: Spectrum of the magnetic field measured in different scenarios with a single MMC sensor using the WiFi method. *Background:* Measure the spectrum at the setup location. *Standby:* Placed an old voltage transformer in standby next to the sensor. *In Action:* Voltage transformer in use with a heating plate connected to it. *Difference Background -Standby:* Difference in amplitude between the background spectrum and the standby spectrum shows a significant peak at 50 Hz for the x and z axis.

high enough to track periodic changes in the magnetic field at 50 Hz.

6 Testing the Cube and the Scaling Method

In this section, we will present multiple experiments conducted with the Cube and the S-06-13-N magnet to test the setup and the scaling method. To that end, we positioned the magnet characterized in section 5.1 in close proximity to the Cube and estimated the direction of its position relative to the center of the Cube by comparing the change in magnitude of the magnetic field measured by the eight sensors.

6.1 Adding Disturbance to Cube Range

First, we tested the scaling method by placing the magnet outside the range of the setup for the reference measurement (approx. 4 m away) and moving it close to the Cube for the
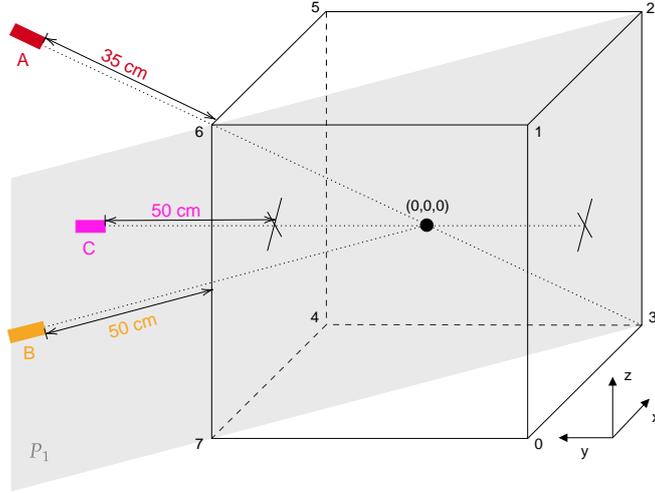
Figure 11: Sketch of the different magnet positions (A - C) tested in the experiment in section 6.1. Positions A and B lie on the plane P_1, whereas C is centered above a face of the Cube. The black numbers indicate the port number of the sensor placed at the corresponding position. The proportions in this sketch are not accurate.

raw measurement. We oriented the magnet such that its cylindrical axis pointed towards the center of the Cube. We repeated this process for various positions of the magnet, illustrated in Figure 11. Each time, the two data sets were taken over a period of 3 s using the WiFi communication method with 33 data points per request. Then, we inferred the direction of the position of the magnet relative to the center of the Cube using the scaling method as outlined in section 4.3.

Following the simulation results from section 4.3, we expect the scaling method to yield accurate results for positions A - C in case of an ideal version of the Cube, as they all lie on symmetry axes of the setup. By 'ideal' we refer to perfectly accurate sensors placed exactly at the corners of a cube. Even though the Cube is not ideal, the results in Figure 12 show a good agreement between the estimated direction according to the scaling method and the actual direction of the magnet for all but one projection of position C. However, even in this case the deviation is small enough to still clearly distinguish position C from A and B and thus get a good indication for the direction of the disturbance.

However, it is important to note, that the accuracy of the scaling method and the Cube is sensitive to the orientation of the magnet. For example, if we rotate the magnet at position C by 90° around the z-axis, the Cube does not register changes in the magnetic field, as they are below 100 nT at all sensor positions.

This orientation sensitivity is also observed, when placing the magnet at position A rotated by 45° in P_1 such that its cylindrical axis lies in the xy-plane and not on the diagonal of the Cube. In this case, the vector obtained with the scaling method does no longer agree with the actual direction of the magnet (see Figure 13), but still points towards the correct face of the Cube.

23
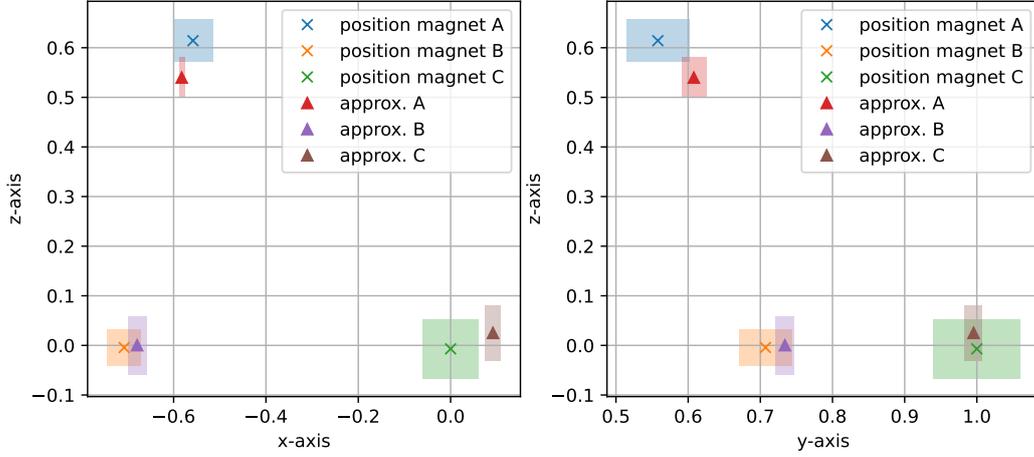
Figure 12: Projection of the direction vector calculated using the scaling method (triangle) compared to the normalized magnet positions (cross), illustrated in Figure 11. Error regions cross: magnet placement uncertainties of $\pm 2\,\mathrm{cm}$ along each axis, re-scaled with absolute value of the position vector. Error regions triangle: error of magnitude from standard deviation of the reference and raw measurements, re-scaled with length of direction vector according to scaling method before normalization. *Left:* xz-plane. *Right:* yz-plane.
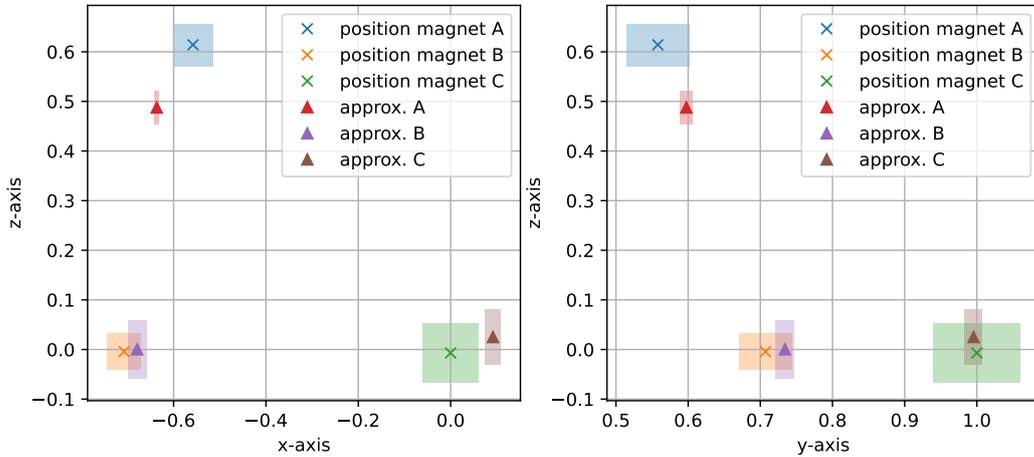
Figure 13: Results of the scaling method if the magnet axis at position A does not point towards the origin but lies in the xy-plane. The results for positions B and C are the same as in Figure 12 and only serve as points of reference. Error regions cross: magnet placement uncertainties of $\pm 2\,\mathrm{cm}$ along each axis, re-scaled with absolute value of the position vector. Error regions triangle: error of magnitude from standard deviation of the reference and raw measurements, re-scaled with length of direction vector according to scaling method before normalization. *Left:* xz-plane. *Right:* yz-plane.

24
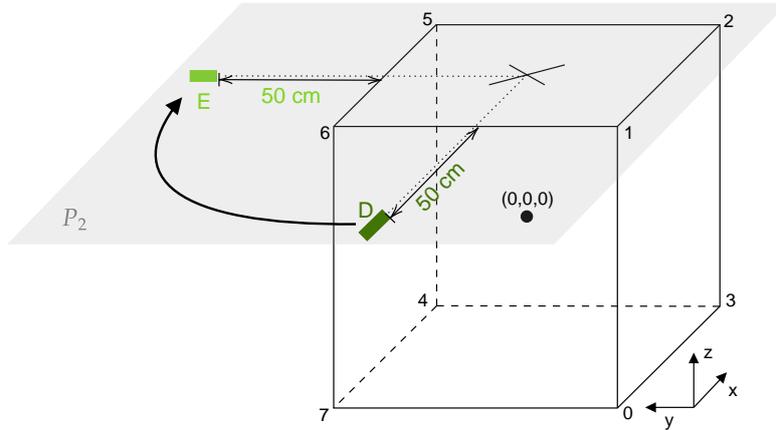
Figure 14: Positions of the test magnet during the reference measurement (D) and the raw data (E) in plane P_2 relative to the Cube. The proportions are not accurate.

6.2 Moving Disturbance in Cube Range

Another possible scenario is a change in position of a magnetic object close to the Cube between the reference measurement and the raw measurement. We tested this scenario with the S-06-13-N magnet by placing it in between sensors 1 and 6 during the reference measurement and in between sensors 5 and 6 during the subsequent raw measurement (see Figure 14), both times at a distance of 50 cm. While the Cube was able to detect a change in the magnetic field, the direction obtained from the scaling method does not agree with the end position E of the magnet as shown in Figure 15. In fact, the resulting vector suggests the magnet to be found at position A, as in the scenario of adding the magnet to the range of the Cube. Consequently, the scaling method is not suitable for determining the direction of a displaced magnetic object in close vicinity of the Cube. Generally speaking, the scaling method yields better results the further away the source of the disturbance is during the reference measurement.
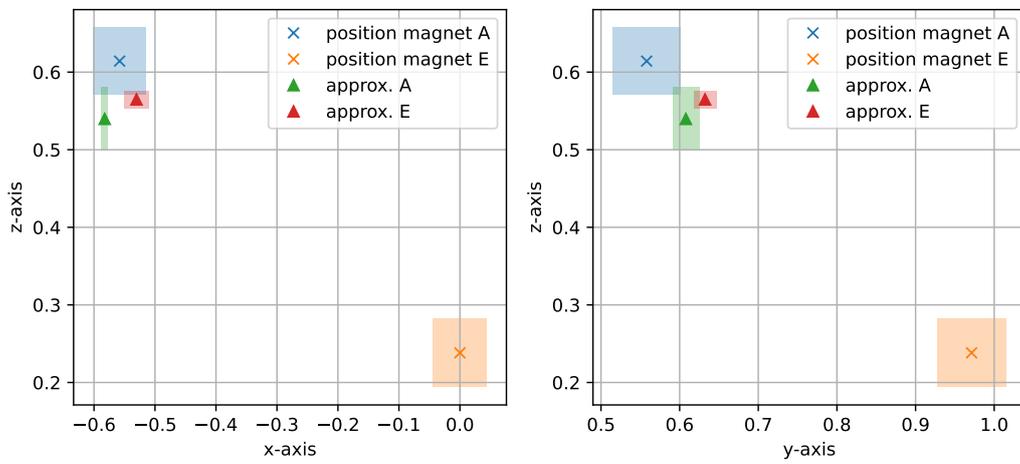
Figure 15: Scaling method results when moving the magnet inside the range of the Cube after the reference measurement. Projection of the direction vector calculated (triangle) compared to the normalized magnet position E and A (cross), illustrated in Figure 14. Error regions cross: magnet placement uncertainties of $\pm 2\,\mathrm{cm}$ along each axis, re-scaled with absolute value of the position vector. Error regions triangle: error of magnitude from standard deviation of the reference and raw measurements, re-scaled with length of direction vector according to scaling method before normalization. *Left:* xz-plane. *Right:* yz-plane.

7   Conclusion and Outlook

In this thesis, we introduced a three-dimensional magnetic field tracking system based on eight magnetic field sensors with a resolution of $\sim 100\,\mathrm{nT}$. We implemented two different data acquisition methods in Python and C++ and characterized two types of magnetic field sensors. Using a straightforward scaling method, we were able to find an accurate estimation of the direction of a test magnet relative to the Cube if placed on a symmetry axis of the setup pointing towards the center of the Cube. However, the performance of the scaling method is limited by factors such as the orientation of the magnet, the distance between the magnet and the Cube during the reference measurement, the resolution of the sensors and the symmetry of the sensor configuration. Possible next steps to improve the design, approximation method and application are:

- **Query Strings:** A significant improvement can be made, by expanding the list of possible client requests to the ESP32, including the use of query strings to set parameters. For example, we could send the number of data points per request as parameter in the http request or define different transmission scenarios for different request messages.

- **Moving average:** Apart from monitoring the magnetic field during an experiment, the Cube could be used to track the magnetic field inside the lab over time. For example, via a moving average.

- **WiFi method:** The main limitations of the WiFi method at the moment are the RAM of the ESP32 and the data point rate. The first problem can be solved by switching to a processor with a higher RAM. In addition, we should be able to increase the data point rate, as the MMC sensors have the capability of measuring the magnetic field vector with a sampling rate of $1\,\mathrm{kHz}$ according to the data sheet.

- **Numerical Approximation:** There is the potential to make estimations of the location and magnetic dipole moment of a disturbance as the Cube measures the magnetic field vector at eight points in space which has not been used in the scaling method. We could test numerical approximation methods to try and infer the position and magnetic moment of the disturbance by approximating its field as magnetic dipole field.

Acknowledgements

First, I would like to thank Dr. Cornelius Hempel for giving me the amazing opportunity to write my semester thesis at his group and Prof. Jonathan Home for officially supervising it. I would also like to thank Jonas Manthey for conceptualizing this project and the support during the first weeks. Special thanks to Michael Marti and Mose Müller for guiding me through this project and always keeping things fun. I owe a huge 'thank you' to Gergö Létay, who sacrificed a weekend to help me with the simulation and provided moral support whenever needed. I also want to express my gratitude to everyone at the ITQC group for their support and for creating such a welcoming atmosphere.

References

[1] J. F. Keithley, *The Story of Electrical and Magnetic Measurements: From 500 B.C. to the 1940s* (John Wiley and Sons, 1999), p.2.

[2] S. Chikazumi, *Physics of Magnetism*, (John Wiley and Sons, Ltd. 1984)

[3] J. D. Jackson, *Classical Electrodynamics*, (Wiley, 1998)

[4] F. Bergamin, *At the frontiers of magnetism*, `https://ethz.ch/en/news-and-events/eth-news/news/2014/05/at-the-frontiers-of-magnetism.html`, (accessed on 06/30/2023)

[5] G. Benenti, G. Casati, G. Strini, *Principles of Quantum Computation and Information*, (World Scientific, 2005). Volume 1: Basic Concepts, p. 100 - 110

[6] J. Stolze, D. Suter, *Quantum Computing - A Short Course from Theory to Experiment*, (WILEY-VCH, 2004)

[7] C. Hempel, *Digital quantum simulation, Schrödinger cat state spectroscopy and setting up a linear ion trap*, PhD thesis, University of Innsbruck, 2014.

[8] R. Oswald, *Characterization and control of a cryogenic ion trap apparatus and laser systems for quantum computing*, PhD thesis, ETH Zurich, 2023

[9] D. J. Griffiths, *Introduction to Electrodynamics*, (PEARSON, Addison Wesley, 1999), Third Edition, p. 202 - 278

[10] J. M. Camacho, V. Sosa (2013), *Alternative method to calculate the magnetic field of permanent magnets with azimuthal symmetry*, Revista mexicana de física E. 59. 8-17.

[11] SparkFun, *Qwiic Products*, `https://www.sparkfun.com/qwiic#products`, (accessed on 06/19/2023)

[12] Espressif Systems, *ESP32-WROOM-32E,ESP32-WROOM-32UE, Datasheet*, `https://www.espressif.com/sites/default/files/documentation/esp32-wroom-32e_esp32-wroom-32ue_datasheet_en.pdf`, Version 1.6, (accessed on 06/06/2023)

[13] InvenSense, Inc., *World's Lowest Power 9-Axis MEMS MotionTracking Device -ICM-20948*, `https://invensense.tdk.com/wp-content/uploads/2016/06/DS-000189-ICM-20948-v1.3.pdf`, Document Number: DS-000189, Revision: 1.3

[14] MEMSIC, Inc., *MEMSIC MMC5983MA Rev A*, `https://cdn.sparkfun.com/assets/2/e/1/8/0/MMC5983MA_RevA_4-3-19.pdf`

[15] Stefan Mayer Instruments, *Fluxgate Magnetometer FLUXMASTER*, `https://www.stefan-mayer.com/images/datasheets/Data-sheet_Fluxmaster.pdf`, (accessed on 17/06/2023)

[16] Webcraft GmbH - supermagnete.ch, *Data sheet article S-06-13-N*, `https://www.supermagnete.de/eng/data_sheet_S-06-13-N.pdf`, (accessed on 06/06/2023)

[17] Webcraft GmbH - supermagnete.ch, *Physical Magnet Data*, `https://www.supermagnete.ch/eng/physical-magnet-data`, (accessed on 06/18/2023)

ETH

Eidgenössische Technische Hochschule Zürich
Swiss Federal Institute of Technology Zurich

Declaration of originality

The signed declaration of originality is a component of every semester paper, Bachelor's thesis, Master's thesis and any other degree paper undertaken during the course of studies, including the respective electronic versions.

Lecturers may also require a declaration of originality for other written papers compiled for their courses.

I hereby confirm that I am the sole author of the written work here enclosed and that I have compiled it in my own words. Parts excepted are corrections of form and content by the supervisor.

Title of work (in block letters):

Localization of Magnetic Field Disturbances using 3-Axis Magnetic Field Sensors

Authored by (in block letters):
For papers written by groups the names of all authors are required.

Name(s):	**First name(s):**
Sanwald	Iva

With my signature I confirm that
- I have committed none of the forms of plagiarism described in the 'Citation etiquette' information sheet.
- I have documented all methods, data and processes truthfully.
- I have not manipulated any data.
- I have mentioned all persons who were significant facilitators of the work.

I am aware that the work may be screened electronically for plagiarism.

Place, date	**Signature(s)**
Zürich, 06.07.23	*J. Sanwald*

For papers written by groups the names of all authors are required. Their signatures collectively guarantee the entire content of the written paper.